Journal of Power Sources 258 (2014) 395–407

Contents lists available at ScienceDirect

Journal of Power Sources

journal homepage: www.elsevier.com/locate/jpowsour

Power split strategies for hybrid energy storage systems for vehicular applications

Alberto Santucci, Aldo Sorniotti*, Constantina Lekakou

University of Surrey, Guildford, UK

HIGHLIGHTS

- A novel model-predictive controller for the energy management of a hybrid energy storage system.
- A novel dynamic programming algorithm maximising battery life along a driving schedule.
- A simulation-based comparison of different controllers for hybrid energy storage systems.
- Evaluation of the energy efficiency properties of the simulated hybrid energy storage system.

ARTICLE INFO

Article history:
Received 17 December 2013
Accepted 30 January 2014
Available online 13 February 2014

Keywords:
Hybrid electric vehicle
Battery
Supercapacitor
Model predictive control
Rule-based control
Dynamic programming

ABSTRACT

This paper deals with the control system development for a hybrid energy storage system, consisting of a battery and a supercapacitor, for a through-the-road-parallel hybrid electric vehicle. One of the main advantages deriving from the coupling of a battery and a supercapacitor is the possibility of reducing battery ageing, in addition to energy efficiency improvements when the system operates in critical climate conditions. At the moment, no specific controller has been proposed with the aim of directly reducing battery wear. This paper presents a novel model predictive controller and a dynamic programming algorithm including a simplified battery ageing model in their formulations. The simulation results of the model predictive controller and dynamic programming algorithm are compared with the results deriving from a rule-based strategy. The rule-based controller achieves a 67% reduction of the root mean square values of battery current along a selection of driving cycles in comparison with the same vehicle equipped with battery only. In the same conditions the battery peak current is reduced by 38%. The model predictive controller and the dynamic programming algorithm further reduce the root mean square value by 6% and 10% respectively, whilst the peak values are additionally decreased by 17% and 45%.

1. Introduction

Supercapacitors are evaluated in automotive industry and academia for hybrid energy storage systems (HESSs), in cooperation with batteries and DC/DC converters. The typical properties [1] of Lithium-Ion batteries and supercapacitors [2] are reported in Table 1.

According to the literature, the first potential benefit of HESSs is represented by the power loss reduction in the energy storage. In fact, the energy efficiency of supercapacitors is higher than for batteries [3,4], especially at significant currents. Moreover, supercapacitors allow regeneration even when the vehicle is working in critical ambient conditions (i.e. at low temperatures [5]), in which the battery cannot operate in regenerative mode. In practical terms, from the analysis of the average working conditions of a vehicle, the supercapacitor contribution in terms of enhanced regeneration is expected to be quite limited. Moreover, in case of HESSs, DC/DC converters [6] are required to decouple the battery and supercapacitor voltage levels. These devices have an efficiency range that at least partially compensates the potential benefit of the supercapacitor when considering the whole system. Within the HESS, the DC/DC converter is usually the interface between the supercapacitor and the DC-link bus voltage, and manages the whole amount of power through the supercapacitor [7]. Schupbach et al. [8] compare different typologies of DC/DC bi-directional converters, in particular half-bridge converters, single-ended primary-inductor converters and Luo converters, reaching the conclusion that the half-bridge layout represents the most efficient option. The same conclusion

* Corresponding author.
E-mail address: a.sorniotti@surrey.ac.uk (A. Sorniotti).

http://dx.doi.org/10.1016/j.jpowsour.2014.01.118
0378-7753

Table 1
Energy storage systems: typical properties.

	Battery	Supercapacitor	Unit
Power density	~1	Up to 20	[kW kg^{-1}]
Energy density	150–200	2–10	[Wh kg^{-1}]
Energy efficiency	75–90	90–98	[%]

is reached by Ref. [9]. A recent paper [10] suggests the installation of the DC/DC converter between the battery and the supercapacitor, and defines four operational modes of the resulting system, controlled through a rule-based algorithm. In conditions of significant power demand and high vehicle speed, the battery is providing energy directly to the motor inverter. This novel solution allows a smaller size of the DC/DC converter in comparison with the conventional HESS layout currently adopted in automotive industry.

Ortuzar et al. [11] report an experimental fuel consumption reduction of about 9% deriving from the adoption of a HESS within a parallel hybrid electric vehicle, however the specific prototype is characterized by a lead-acid battery, notoriously less efficient than modern Lithium-Ion batteries. A similar study [12] estimates energy consumption reductions of 15–20% through the HESS, but also in this case a lead-acid battery is considered, while in Ref. [13] the efficiency improvement is between 4 and 13% depending on the driving schedule. A very recent paper [14], based on vehicle simulations, shows significant energy consumption benefits (from 27% to 42% depending on the driving schedule) deriving from the adoption of a HESS on a series hybrid electric bus. However, the DC/DC converter efficiency does not seems to be considered in the simulation model of the power system. Moreover, the implemented algorithm guarantees the charge sustainability of the supercapacitor during the driving schedule, but no reference is made to the charge sustainability of the battery, nor to any compensation of the fuel consumption for considering the difference in battery state of charge between the initial and final conditions. Therefore, a rigorous comparison of the actual power losses for vehicle applications with HESS and with battery only is still required.

The second (but potentially more important than the first one) benefit of supercapacitors is represented by the reduction of battery dynamic loads (i.e. currents) [15], which have direct impact on battery life expectancy. According to the preliminary analysis of [16], based on experimental lead-acid battery data from Refs. [17] and [18], HESSs bring a potential increase of battery life between 137% (for traction batteries) and 253% (for starter batteries). However, a direct estimation of modern Lithium-Ion battery life extension due to the adoption of a HESS is still missing in the literature, together with an on-line control formulation of the power split between battery and supercapacitor, directly considering battery wear. Several simulation studies present various forms of empirical battery models [19,20], which are suitable for a computationally efficient estimation of battery wear for control purposes. In general, battery wear depends on the current profile, the depth of discharge (i.e. the same current profile provokes more wear at low state of charge) and thermal conditions. Masih-Tehrani et al. [14] adopt a specific wear model for $LiFePO_4$ batteries in order to develop a dynamic programming algorithm based on the minimization of the management cost of a hybrid electric vehicle, including fuel consumption and periodic battery substitutions. However, the calendar life of the battery is not considered and the amount of increase of battery life is not explicitly presented.

A variety of controllers for HESSs are discussed in the literature. For example, in the area of heuristic controllers:

i) the 'all or nothing' strategy, which uses the supercapacitor (and not the battery) when its state of charge is above an assigned critical level, and only uses the battery when the supercapacitor is discharged [21];
ii) a strategy similar to i), however providing a smooth transition between the areas covered by one component only. The weighting factor of the power contribution of the battery and supercapacitor is based on a look-up table as a function of the supercapacitor state of charge [21];
iii) a strategy based on a bi-dimensional look-up table, computing the power fraction to the battery as a function of the states of charge of the battery and supercapacitor [21];
iv) the filtration strategy, based on the low-pass filtering of the traction current for the computation of the battery contribution, whilst the supercapacitor contribution derives from the high-pass filtering of the traction current [21,22];
v) a vehicle speed-based strategy, according to which the supercapacitor is charged up to full capacity during periods of low vehicle speed such that it is ready to provide power during acceleration. Conversely, during periods of high vehicle speed, the ultracapacitor should be at the lowest desired state of charge in order to fully accept regenerative charge during a braking event. An empirical formula establishing the relationship between the supercapacitor reference voltage and vehicle speed is provided in Ref. [11]. Ref. [23] adds a rule to the speed-based strategy, in order to explicitly limit the peaks of battery current. Ref. [24] uses the same empirical formula for calculating the reference voltage of the supercapacitor, and then a proportional controller based on the difference between the reference and actual supercapacitor voltage is adopted for the calculation of the supercapacitor power;
vi) a rule-based strategy based on the combination of i)–v), with the rules taking into account the state of charge of the two components and the HESS current demand, with an implicit limitation of the battery current profile (despite no filter is included). The authors of this algorithm [16] insist (without quantitative figures) on the potential life extension of the battery as the main consequence of the adoption of the HESS and the proposed controller.

In Ref. [21] strategies i)–iii) are compared against each other in terms of battery current profile, and iii) provides the smoothest profile, however the battery model adopted for the assessment of the controllers does not contain an explicit calculation of battery wear.

Borhan et al. [25] describe a model predictive controller (MPC) for the power split between battery, supercapacitor and internal combustion engine in a hybrid electric vehicle. However, the control structure integrates the drivetrain power split (i.e. the one between engine and electric motor) and the HESS power split into a single controller, which is not industrially viable. In fact, the same hybrid electric vehicle should undergo a redesign of its whole powertrain controller, when passing from a battery only energy storage to a HESS, without any modification of the hybrid powertrain. The same limitation applies to the Pontryagin's minimum principle-based controller presented in Ref. [12], which is run offline for computational reasons. Moreover, the MPC in Ref. [25] is designed for tracking a reference state of charge of the supercapacitor, which is not clearly specified in the paper. Finally, Ref. [11] proposes a neural network-based strategy, with the specific purpose of reducing the power losses in the HESS.

The conclusion is that there is no wide consensus regarding the assessment of the actual main benefit deriving from the adoption of the HESS (efficiency or battery wear reduction), nor any on-line HESS management algorithm designed to explicitly take into account battery wear.

The objectives of this paper are:

- To formulate an innovative model predictive controller for hybrid electric or fully electric vehicle HESS management, specifically designed for the reduction of battery wear;
- To design a novel dynamic programming (DP) formulation for estimating the ideally achievable increase of battery life duration through the HESS. Simplified forms of DP can become viable in future by using the information from the cloud [26] and the vehicle navigation system for programming the schedule of the whole trip;
- To assess the performance benefits (i.e. battery life extension and power losses) of MPC and DP against a computationally efficient rule-based algorithm from the literature (formulation vi) discussed in this section), and outline the trade-off between model-based controllers and heuristic formulations for HESS management;
- To compare the energy storage power losses in case of battery only and of HESS, for a case study through-the-road-parallel (TTRP) hybrid electric vehicle (HEV) along a selection of driving cycles.

The paper presents the simulation model including the high-level controller for the power split between battery and supercapacitor, three formulations of HESS management controllers for the increase of battery life expectancy, and a detailed analysis of the simulation results.

2. Simulation model and high-level controller

2.1. Vehicle model

The case study vehicle is a high performance passenger car consisting of a front electric axle equipped with a 2-speed transmission system [27] and a rear engine-driven axle equipped with a 7-speed dual clutch gearbox [28]. The vehicle layout is shown in Fig. 1, while the main vehicle parameters are reported in Table 2. The simulator (Fig. 2) is based on a hybrid backward/forward-facing approach [29] that allows the calculation of the amount of energy/power required from the HESS along the driving schedule.

The overall drivetrain torque at the wheel, T_W, can be calculated as the sum of the internal combustion engine (ICE) drivetrain torque, $T_{W_{ICE}}$, and the electric motor (EM) drivetrain torque, $T_{W_{EM}}$:

$$T_W(t) = T_{W_{EM}}(t) + T_{W_{ICE}}(t) \tag{1}$$

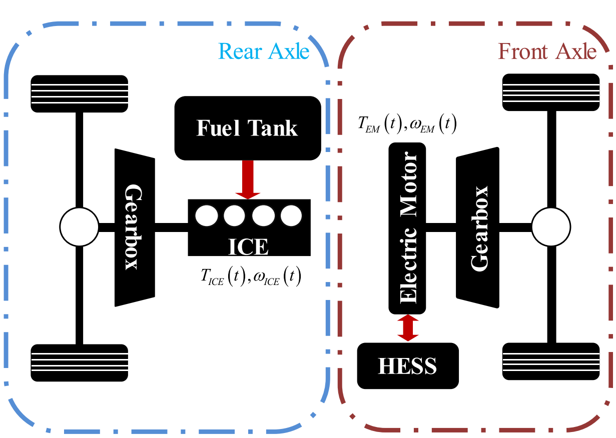

Fig. 1. TTRP HEV layout.

Table 2
Main vehicle parameters.

Symbol	Description	Quantity	Unit
M	Overall vehicle mass (unladen)	2036	[kg]
l	Wheelbase	2.99	[m]
h_{CG}	Height of the centre of mass	0.47	[m]
C_d	Aerodynamic drag coefficient	0.35	[−]
S	Frontal area	2.24	[m^2]
ω_{EMmax}	Maximum electric motor speed	12,000	[rpm]
T_{EMmax}	Maximum electric motor torque	120	[Nm]
ω_{ICEmax}	Maximum internal combustion engine speed	8000	[rpm]
T_{ICEmax}	Maximum internal combustion engine torque	683	[Nm]

$T_{W_{ICE}}$ is given by:

$$T_{W_{ICE}}(t) = T_{ICE}\tau_{GB_{ICE}}\tau_{Diff_{ICE}}\eta_{GB_{ICE}}\eta_{Diff_{ICE}} - J_{eq_{ICE}}\ddot{\vartheta}_W \tag{2}$$

where T_{ICE} is the engine torque, $\tau_{GB_{ICE}}$ is the ICE axle gearbox ratio, $\tau_{Diff_{ICE}}$ is the ICE differential gear ratio, $\eta_{GB_{ICE}}$ is the ICE gearbox efficiency, $\eta_{Diff_{ICE}}$ is the ICE final reduction efficiency, $J_{eq_{ICE}}$ is the equivalent inertia of the ICE drivetrain at the wheel and $\ddot{\vartheta}_W$ is wheel acceleration. A first approximation of $J_{eq_{ICE}}$ can be calculated as:

$$\begin{aligned} J_{eq_{ICE}} &= J_W + J_{Diff_{ICE}} + J_{SS_{ICE}}\tau_{Diff_{ICE}}^2\eta_{Diff_{ICE}} \\ &\quad + J_{PS_{ICE}}\tau_{GB_{ICE}}^2\tau_{Diff_{ICE}}^2\eta_{GB_{ICE}}\eta_{Diff_{ICE}} \end{aligned} \tag{3}$$

where J_W is the wheel inertia, $J_{Diff_{ICE}}$ is the ICE differential assembly inertia, $J_{SS_{ICE}}$ is the ICE secondary shaft equivalent inertia and $J_{PS_{ICE}}$ is the ICE primary shaft equivalent inertia. Similarly, $T_{W_{EM}}$ is given by:

$$T_{W_{EM}}(t) = T_{EM}\tau_{GB_{EM}}\tau_{Diff_{EM}}\eta_{GB_{EM}}\eta_{Diff_{EM}} - J_{eq_{EM}}\ddot{\vartheta}_W \tag{4}$$

where T_{EM} is the electric motor torque, $\tau_{GB_{EM}}$ is the EM axle gearbox ratio, $\tau_{Diff_{EM}}$ is the EM differential gear ratio, $\eta_{GB_{EM}}$ is the EM gearbox efficiency, $\eta_{Diff_{EM}}$ is the EM final reduction efficiency and $J_{eq_{EM}}$ is the equivalent inertia of the EM drivetrain at the wheel. A first approximation of $J_{eq_{EM}}$ can be calculated as:

$$\begin{aligned} J_{eq_{EM}} &= J_W + J_{Diff_{EM}} + J_{SS_{EM}}\tau_{Diff_{EM}}{}^2\eta_{Diff_{EM}} \\ &\quad + J_{PS_{EM}}\tau_{GB_{EM}}{}^2\tau_{Diff_{EM}}{}^2\eta_{GB_{EM}}\eta_{Diff_{EM}} \end{aligned} \tag{5}$$

where $J_{Diff_{EM}}$ is the EM differential inertia, $J_{SS_{EM}}$ is the EM secondary shaft equivalent inertia and $J_{PS_{EM}}$ is the EM primary shaft equivalent inertia. The drivetrain efficiencies are implemented in the form of look-up tables (experimentally derived by the respective manufacturers) as functions of input torque, speed and operating temperature. The wheel and vehicle balance equations are omitted for brevity. Gearshift maps are adopted for the transmission gear selection.

2.2. High-level controller

The high-level controller has to determine the power split between the ICE driven axle and the EM driven axle of the TTRP HEV. The adopted algorithm is the equivalent consumption minimization strategy (ECMS) presented in Refs. [30,31]. Alternative formulations are presented and discussed in the literature [32,33].

The core of the strategy is the cost function (Eq. (6)), defined as the sum of the fuel cost (dimensionally a fuel mass flow rate) and the equivalent cost of the electric energy. At each time step the costs for all the feasible splits are evaluated and the power split with the minimum cost is selected.

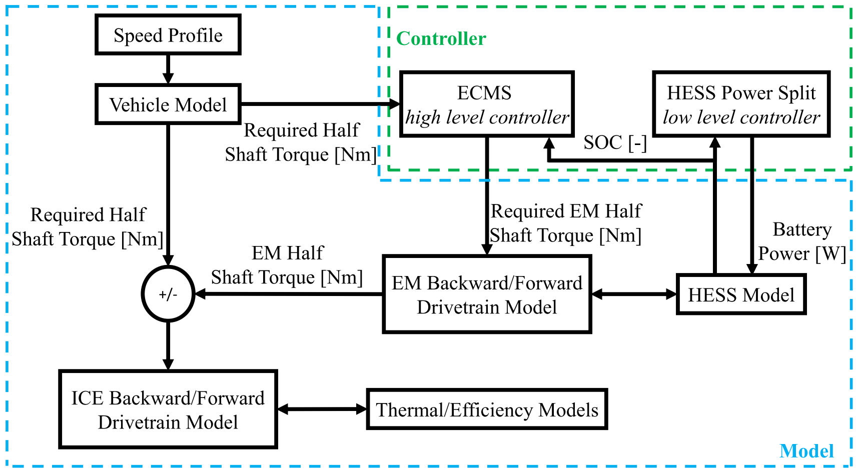

Fig. 2. Schematic of the vehicle simulator.

$$C(t) = C_{EM}(t) + C_{ICE}(t) \tag{6}$$

where $C_{EM}(t)$ (Eq. (7), in which the two formulations refer to positive and negative motor torques) is the cost related to the electric drivetrain and $C_{ICE}(t)$ (Eq. (8)) is the cost related to the ICE drivetrain:

$$C_{EM}(t) = \begin{cases} \frac{SFC_D P_{EM}(T_{EM}(t),\omega_{EM}(t))}{\overline{\eta}_{EM}\overline{\eta}_{HESS}} \\ SFC_R P_{EM}(T_{EM}(t),\omega_{EM}(t))\overline{\eta}_{HESS}\overline{\eta}_{EM} \end{cases} \tag{7}$$

$$C_{ICE}(t) = BSFC_{MAP}(T_{ICE}(t),\omega_{ICE}(t))\cdot P_{ICE}(t) \tag{8}$$

where $\overline{\eta}_{HESS}$ and $\overline{\eta}_{EM}$ are respectively the lumped average efficiency of the HESS and EM drivetrains, SFC_R and SFC_D are respectively the equivalent cost factors during HESS charge and discharge, P_{EM} is the EM power, T_{ICE}, ω_{ICE} and P_{ICE} are respectively the ICE torque, speed and power, and $BSFC_{MAP}$ is the ICE brake specific fuel consumption.

The algorithm selects the feasible split with the minimum cost, C^*:

$$C^* = \min[C(t)] \tag{9}$$

2.3. Hybrid energy storage system

The HESS model includes the battery and supercapacitor models, which are connected in parallel with the DC/DC converter, as shown in Fig. 3.

2.3.1. Battery model

The battery model (Fig. 4) implemented in the vehicle simulator is described in Ref. [34]. This model has been selected because it has already been experimentally validated for several commercial Lithium-Ion batteries (e.g. Sony US18650, Panasonic CGR18650) and because of its low computational cost.

The model is based on: i) an equilibrium potential, E_{Batt}, defined by a look-up table as a function of temperature and state of charge; ii) two resistors, $R_{1,Batt}$ and $R_{2,Batt}$, for the computation of the power losses; and iii) a capacitance, C_{Batt}, which characterizes the transient response of the battery. The state of charge (SOC_{Batt}) is computed as:

$$SOC_{Batt} = \frac{1}{Q}\int_0^{t_{sim}} \alpha(I_{Batt})\beta(T_{Batt})I_{Batt}(t)dt + SOC_{0,\,Batt} \tag{10}$$

where Q is the battery capacity, $\alpha(I_{Batt})$ takes into account the charge/discharge rate effect, $\beta(T_{Batt})$ takes into account the thermal effect, I_{Batt} and T_{Batt} are respectively battery current and temperature, and $SOC_{0,Batt}$ is the initial state of charge. The main battery cell parameters (Dow Kokam XALT 8 Ah) considered in this activity are reported in Table 3.

Since the battery behaviour is temperature dependent, a thermal model is required. An approximated thermal energy balance has been adopted [35].

$$\begin{aligned} m\cdot c_P\cdot\frac{dT_{Batt}(t)}{dt} &= I_{Batt}(t)^2\cdot R_{2,\,Batt} + \frac{1}{R_{1,\,Batt}} \\ &\quad [V_{Batt}(t) - E_{Batt}(t) - R_{2,\,Batt}I_{Batt}]^2 \\ &\quad - h_cA[T_{Batt}(t) - T_a] \end{aligned} \tag{11}$$

where m is the mass of the battery, c_P is the specific heat capacity, T_{Batt} is the battery temperature, V_{Batt} is the potential

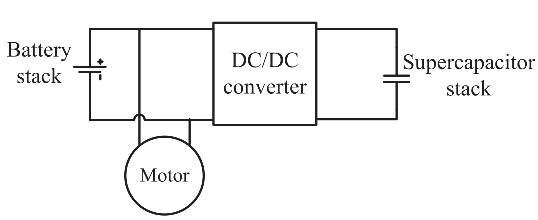

Fig. 3. Simulated HESS layout.

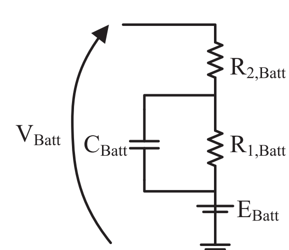

Fig. 4. Equivalent battery model.

Table 3
Battery cell parameters.

Description	Quantity	Unit
Nominal cell capacity	8	[Ah]
Nominal cell voltage	3.7	[V]
Peak cell discharging current	24	[A]
Number of cells in parallel	6	[–]
Number of cells in series	82	[–]

across the battery terminals, h_c is the convective heat transfer coefficient, A is the equivalent surface and T_a is the ambient temperature.

To evaluate the battery wear during the driving cycle, a damage accumulation model, namely "accumulated Ah-throughput" [36], has been implemented. It is based on the total amount of charge that can flow through the battery before it reaches the end of its life. The model relies on the definition of a severity factor σ (Eq. (12)), which depends on I_{Batt}, T_{Batt} and SOC_{Batt}:

$$\sigma = \frac{\gamma(I_{Batt}, T_{Batt}, SOC_{Batt})}{\Gamma} = \frac{\int_0^{EOL} |I_{Batt}| dt}{\int_0^{EOL} |I_{nom}| dt} \quad (12)$$

where $\gamma(I_{Batt}, T_{Batt}, SOC_{Batt})$ is the battery duration (Ah-throughput) corresponding to its actual operating conditions in terms of current, temperature and state of charge, Γ is the total Ah-throughput when the battery undergoes nominal cycles, as defined by the manufacturer (in the case study the nominal conditions are 1-C rate, 25 °C and 100% depth of discharge). I_{nom} is the nominal current and EOL indicates the end of life. The severity factor represents the relative ageing effect with respect to the nominal cycle, and is higher than 1 for conditions which are more demanding in terms of battery wear. A qualitative example of severity factor map is provided in Fig. 5. Low operating temperatures, low values of SOC_{Batt} and high C-rates provoke a significant increase of the severity factor. These maps can be obtained through specific experimental procedures, which, however, are beyond the common practices of battery manufacturers [36]. This uncertainty in the severity factor determination is the reason why the benefits deriving from the adoption of a HESS are usually presented in terms of reduction of battery current, and not directly in terms of battery life. However, the analysis of the HESS performance should be actually based on the extension of battery life.

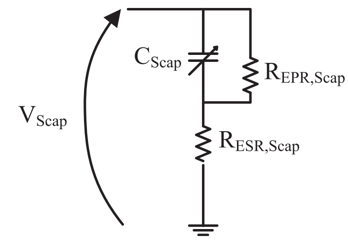

Fig. 6. Equivalent supercapacitor circuit.

To evaluate the actual depletion of the battery charge, the following equation is adopted:

$$Ah_{eff} = \int_0^t \sigma(I_{Batt}, T_{Batt}, SOC_{Batt}) |I_{Batt}(\tau)| d\tau \quad (13)$$

which represents the amount of charge that would need to go through the battery using the nominal cycle to have the same ageing effect of the actual conditions. The end of life is reached when $Ah_{eff} = \Gamma$ [36].

2.3.2. *Supercapacitor model*

The supercapacitor is modelled by a series resistance $R_{ESR,Scap}$, the main responsible for the losses in the component, a capacitance C_{Scap}, and a resistor $R_{EPR,Scap}$ to model the self-discharge current. The capacitor is characterized by a variable capacitance which is dependent on its cross voltage.

This model (Fig. 6) has been chosen because of its flexibility and low computational cost, nevertheless, it is well known in literature [37,38]. The parameters of the circuit (referring to the NESSCAP supercapacitor 5000 F), included in Table 4, can be derived from a set of charge-discharge tests [39].

2.3.3. *DC/DC converter model*

In order to take in account the losses in the DC/DC converter an efficiency map has been adopted. This map is a function of the supercapacitor voltage and power demand [22].

3. HESS controllers

3.1. *Rule-based strategy [16]*

The flow-chart describing the rule-based strategy, presented in Ref. [16], is reported in Fig. 7. The algorithm decides the power split depending on the overall power request and the state of charge of

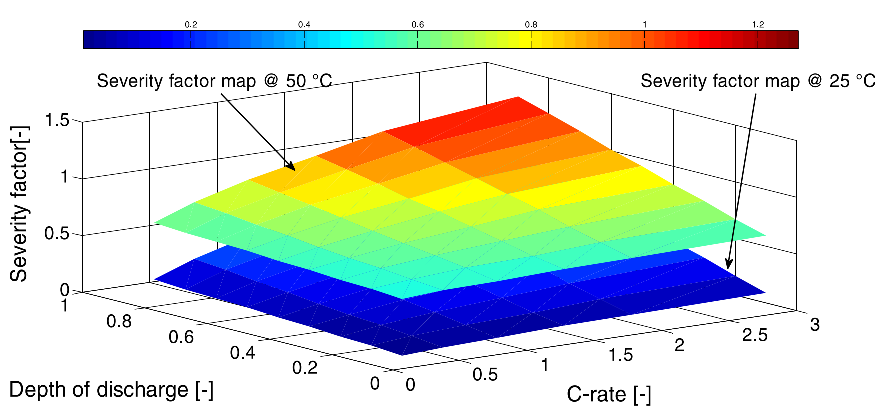

Fig. 5. Battery severity factor map.

Table 4
Supercapacitor cell parameters.

Description	Quantity	Unit
Nominal cell capacitance	5000	[F]
Rated cell voltage	2.7	[V]
Peak cell current	2547	[A]
Number of cells in series	112	[−]

the supercapacitor. P_{min} is the battery power threshold (in discharge) below which the whole power demand is met by the battery, P_{ch} is the charging power sent from the battery to the supercapacitor, and V_{req} is the required supercapacitor voltage, which is a decreasing function of vehicle speed.

Rule-based controllers are easily implementable; however significant care is required in the empirical tuning of their parameters. Some examples of sensitivity analysis of the impact of the main tuning factors are discussed here. The increase of predicted battery life as a function of P_{min} is shown in Fig. 8. The battery life peaks at around 6000 W for all the simulated driving cycles, value at which the battery root mean square (RMS) current also shows a minimum (Fig. 9). Finally, the maximum value of the battery current for all the driving schedules simulated as function of P_{min} is reported in Fig. 10. In summary, a good trade-off for the parameter P_{min} is represented by 6000 W, therefore this value has been selected for the final simulations and comparison with the other controllers. Moreover, a sensitivity analysis of P_{ch} has been carried out (here omitted for brevity). However, its impact on the predicted battery life, RMS and maximum current can be neglected.

In summary, the main controller parameters adopted in this study are reported in Table 5. The sampling time of the controller has been set at the same value as the sampling time of the HESS model (0.01 s).

3.2. Model predictive control

The MPC algorithm involves three steps (Fig. 11): i) prediction of the future outputs over the optimisation horizon, using a simplified model of the system; ii) evaluation of the cost function for the set of future outputs of the system; and iii) adoption of the control policy with the minimum cost and compliant with the system constraints.

The controller relies on a model of the system and a cost function, which represent the core of the algorithm. The model has to predict the system response with good accuracy, while keeping a low computational cost. In this study, reduced order models of the HESS components have been adopted as reported in the following paragraphs.

The proposed MPC has a lower hierarchical level than the ECMS controller in the overall system of Fig. 2. This hierarchical structure

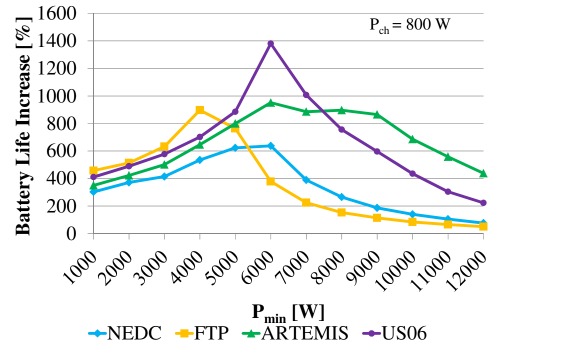

Fig. 8. Battery life increase as function of the tuning parameter P_{min} for the different driving cycles.

makes the controller more practical for a real world vehicle implementation than the one presented in Ref. [25], including the overall energy management and the HESS management in a single control structure.

3.2.1. Battery model

The battery model for MPC design is reported in Fig. 12. It is based on the battery equilibrium potential, E_{Batt}, and an equivalent internal resistance, R_{Batt}. The component dynamics can be derived from the battery power, P_{Batt}:

$$P_{Batt} = R_{Batt} I_{Batt}^2 + E_{Batt} I_{Batt} \tag{14}$$

$$I_{Batt} = \frac{-E_{Batt} + \sqrt{E_{Batt}^2 + 4R_{Batt}P_{Batt}}}{2R_{Batt}} \tag{15}$$

$$\dot{SOC}_{Batt} = \frac{dSOC_{Batt}}{dt} = \frac{I_{Batt}}{Q} = \frac{-E_{Batt} + \sqrt{E_{Batt}^2 + 4R_{Batt}P_{Batt}}}{2R_{Batt}Q} \tag{16}$$

3.2.2. Supercapacitor model

The supercapacitor dynamics, deriving from the simplified model in Fig. 13, can be expressed as:

$$P_{Scap} = R_{Scap} I_{Scap}^2 + V_C I_{Scap} \tag{17}$$

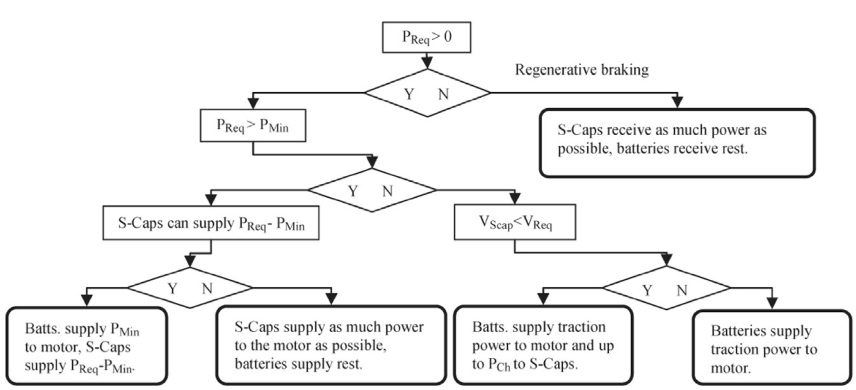

Fig. 7. Rule-based strategy flow-chart [16].

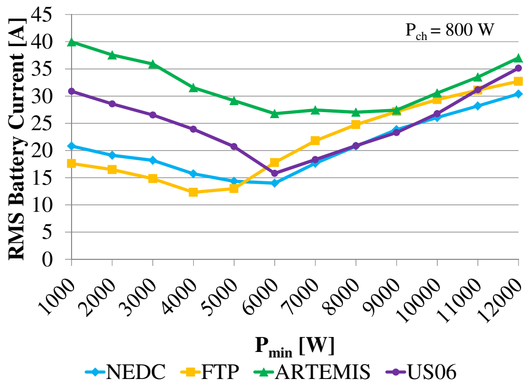

Fig. 9. Root mean square battery current as function of the tuning parameter P_{min} for the different driving cycles.

$$I_{Scap} = \frac{-SOC_{Scap}V_{c,\,max} + \sqrt{\left(SOC_{Scap}V_{c,\,max}\right)^2 + 4R_{Scap}P_{Scap}}}{2R_{Scap}} \tag{18}$$

$$\dot{SOC}_{Scap} = \frac{dSOC_{Scap}}{dt} = \frac{d\left(\frac{C_{Scap}V_C}{C_{Scap}V_{c,\,max}}\right)}{dt} = \frac{-SOC_{Scap}V_{c,\,max} + \sqrt{\left(SOC_{Scap}V_{c,\,max}\right)^2 + 4R_{Scap}P_{Scap}}}{2R_{Scap}V_{c,max}C_{Scap}} \tag{19}$$

where I_{Scap} is the supercapacitor current, V_C is the voltage across the capacitance, R_{Scap} is the supercapacitor resistance, SOC_{Scap} is the supercapacitor state of charge and $V_{c,max}$ is the maximum capacitance voltage.

3.2.3. Controller implementation

Within the implicit MPC algorithm a state-space representation of the system has been implemented [40]. The states x, the inputs u and the outputs y of the state-space formulation are reported in Eq. (20).

$$x = \begin{Bmatrix} SOC_{Scap} \\ SOC_{Batt} \end{Bmatrix}, \quad u = \begin{Bmatrix} P_{Scap} \\ P_{Batt} \end{Bmatrix}, \quad y = \begin{Bmatrix} SOC_{Scap} \\ \sigma I_{Batt} \end{Bmatrix} \tag{20}$$

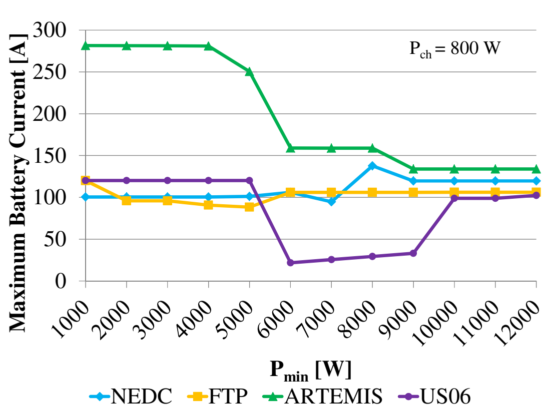

Fig. 10. Maximum battery current as function of the tuning parameter P_{min} for the different driving cycles.

Table 5
Rule-based controller parameters.

Symbol	Quantity	Value	Unit
P_{ch}	Minimum battery power	800	[W]
P_{min}	Power delivered by the battery to the supercapacitor	6000	[W]
SOC_{max}	Maximum supercapacitor state of charge	1	[–]
SOC_{min}	Minimum supercapacitor state of charge	0.5	[–]

At each sample time k the system equations and the characteristics (i.e. $E_{Batt}(SOC_{Batt})$) of the components are linearized around the operating conditions at the beginning of the control window. The dynamics of the system can be expressed as:

$$\begin{Bmatrix} \dot{SOC}_{Scap} \\ \dot{SOC}_{Batt} \end{Bmatrix} = \begin{bmatrix} A_{Scap} & 0 \\ 0 & A_{Batt} \end{bmatrix} \begin{Bmatrix} SOC_{Scap} \\ SOC_{Batt} \end{Bmatrix} + \begin{bmatrix} B_{Scap} & 0 \\ 0 & B_{Batt} \end{bmatrix} \times \begin{Bmatrix} P_{Scap} \\ P_{Batt} \end{Bmatrix} + \begin{bmatrix} K_{Scap} \\ K_{Batt} \end{bmatrix} \tag{21}$$

while the outputs of the system are formulated as:

$$\begin{Bmatrix} SOC_{Scap} \\ \sigma I_{Batt} \end{Bmatrix} = \begin{bmatrix} C_{Scap} & 0 \\ 0 & C_{Batt} \end{bmatrix} \begin{Bmatrix} SOC_{Scap} \\ SOC_{Batt} \end{Bmatrix} + \begin{bmatrix} 0 & 0 \\ 0 & D_{Batt} \end{bmatrix} \times \begin{Bmatrix} P_{Scap} \\ P_{Batt} \end{Bmatrix} + \begin{bmatrix} 0 \\ K'_{Batt} \end{bmatrix} \tag{22}$$

where K_{Scap}, K_{Batt} and K'_{Batt} are constant matrices deriving from the system linearization. By defining the matrices in Eq. (23) and in Eq. (24):

$$A = \begin{bmatrix} A_{Scap} & 0 \\ 0 & A_{Batt} \end{bmatrix}, \quad B = \begin{bmatrix} B_{Scap} \\ B_{Batt} \end{bmatrix} \tag{23}$$

$$\Psi = \begin{bmatrix} A \\ \vdots \\ A^{t_w} \\ A^{t_w} \\ \vdots \\ A^{t_p} \end{bmatrix}, \quad \Gamma = \begin{bmatrix} B \\ \vdots \\ \sum_{i=0}^{t_w-1} A^iB \\ \sum_{i=0}^{t_w} A^iB \\ \vdots \\ \sum_{i=0}^{t_p-1} A^iB \end{bmatrix} \tag{24}$$

where t_w is the length of the control window and t_p is the prediction time, the free evolution of the system states over the prediction time, $x(k)$, can be expressed as:

$$x(k) = k[\Psi\{x\} + \Gamma P_{Batt}(k-1) + K] + x_0 \tag{25}$$

x_0 contains the initial conditions at the beginning of the control window, k is the time instant over the prediction time and K contains constants deriving from the linearization of the system.

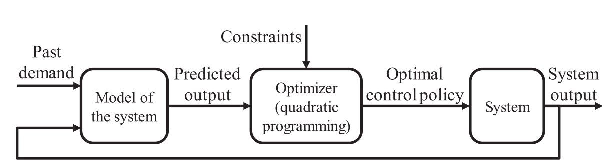

Fig. 11. MPC algorithm layout.

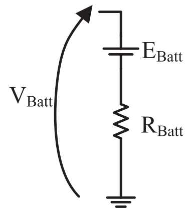

Fig. 12. Equivalent battery model for MPC controller design.

The cost function $J_{\mathrm{MPC}}(k)$ to be minimised along the control horizon is:

$$J_{\mathrm{MPC}}(k) = \sum_{j=\frac{t_s}{\Delta t}}^{\frac{t_s+t_p}{\Delta t}} \left[\|Y(j) - T(j)\|_Q^2 + \|\Delta P_{\mathrm{Batt}}(j)\|_R^2 \right] \tag{26}$$

where j indicates a sample of the prediction, which is discretised at time intervals Δt (they can be different from the discretisation time adopted for k), t_s represents the beginning of the control window, $Y(j)$ is the actual output of the system, $T(j)$ is the reference output of the system, and Q and R are two weighting matrices.

By defining $\varepsilon(k)$:

$$\varepsilon(k) = T(k) - \begin{bmatrix} 1 \\ \sigma_{\mathrm{fr}}(k) \\ \vdots \\ 1 \\ \sigma_{\mathrm{fr}}(k) \end{bmatrix} [\Lambda x(k) + \Xi P_{\mathrm{Batt}}(k-1)] \tag{27}$$

where σ_{fr} is the battery severity factor (Eq. (12)) evaluated for the free response of the system, the second term on the right-hand side of Eq. (27) represents the free response of the system outputs. The matrices Λ and Ξ are reported in Eq. (28):

$$\Lambda = \begin{bmatrix} C & 0 & 0 \\ 0 & \ddots & 0 \\ 0 & 0 & C \end{bmatrix}, \ \Xi = \begin{bmatrix} D \\ \vdots \\ D \end{bmatrix} \tag{28}$$

where the matrices C and D (from the state-space formulation of Eq. (22)) are expressed in Eq. (29):

$$C = \begin{bmatrix} C_{\mathrm{Scap}} & 0 \\ 0 & C_{\mathrm{Batt}} \end{bmatrix}, \ D = \begin{bmatrix} 0 \\ D_{\mathrm{Batt}} \end{bmatrix} \tag{29}$$

The forced response E of the system outputs can be written as:

$$E = \theta \Delta P_{\mathrm{Batt}}(k) \tag{30}$$

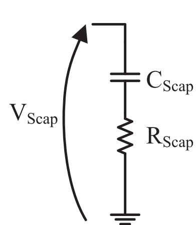

Fig. 13. Equivalent supercapacitor model for MPC controller design.

in which θ is expressed by:

$$\theta = \begin{bmatrix} B_{\mathrm{Scap}} & \cdots & 0 \\ \sigma_{\mathrm{m}} D_{\mathrm{Batt}} & 0 & 0 \\ A_{\mathrm{Scap}} B_{\mathrm{Scap}} + B_{\mathrm{Scap}} & \cdots & 0 \\ 0 & \cdots & 0 \\ \vdots & \ddots & \vdots \\ \sum_{i=0}^{t_w-1} A_{\mathrm{Scap}}{}^i B_{\mathrm{Scap}} & \cdots & B_{\mathrm{Scap}} \\ 0 & \sigma_{\mathrm{m}} D_{\mathrm{Batt}} & 0 \\ \sum_{i=0}^{t_w} A_{\mathrm{Scap}}{}^i B_{\mathrm{Scap}} & \cdots & A_{\mathrm{Scap}} B_{\mathrm{Scap}} + B_{\mathrm{Scap}} \\ 0 & \cdots & 0 \\ \vdots & \vdots & \vdots \\ \sum_{i=0}^{t_p-1} A_{\mathrm{Scap}}{}^i B_{\mathrm{Scap}} & \cdots & \sum_{i=0}^{t_p-t_w} A_{\mathrm{Scap}}{}^i B_{\mathrm{Scap}} \\ 0 & 0 & \sigma_{\mathrm{m}} D_{\mathrm{Batt}} \end{bmatrix} \tag{31}$$

σ_{m} is the average value of the severity factor over the prediction time. The cost function can be re-written as:

$$J_{\mathrm{MPC}}(k) = \varepsilon(k)^T Q \varepsilon(k) - \Delta P_{\mathrm{Batt}}(k)^T G + \Delta P_{\mathrm{Batt}}(k)^T L \Delta P_{\mathrm{Batt}}(k) \tag{32}$$

where ΔP_{Batt} is the battery power difference between two consecutive time samples. G is defined as [40]:

$$G = 2\theta^T Q \varepsilon(k) \tag{33}$$

and L as:

$$L = \theta^T Q \theta + R \tag{34}$$

Therefore, the cost function (Eq. (32)) is the sum of the free evolution of the system ($\varepsilon(k)^T Q \varepsilon(k)$) and the term to be minimized ($\Delta P_{\mathrm{Batt}}(k)^T G + \Delta P_{\mathrm{Batt}}(k)^T L \Delta P_{\mathrm{Batt}}(k)$), physically representing the forced response of the system. This results in a quadratic programming problem (Eq. (35)) for which efficient on-line computational techniques are available, such as interior point [41] and active set [42]:

$$J^*_{\mathrm{MPC,\,Opt}}(k) = \min \left[\frac{1}{2} \Delta P_{\mathrm{Batt}}(k)^T H \Delta P_{\mathrm{Batt}}(k) + f^T \Delta P_{\mathrm{Batt}}(k) \right] \tag{35}$$

$$A_{\mathrm{constr}} \Delta P_{\mathrm{Batt}}(k) \le B_{\mathrm{constr}} \tag{36}$$

where A_{constr} and B_{constr} are the two constraint matrices (i.e. defining the minimum and maximum state of charge for the supercapacitor and the battery), and H and f are two matrices deriving from the quadratic programming formulation [40].

The reference values for the controller in $Y(j)$ (Eq. (26)) are the supercapacitor state of charge ($\mathrm{SOC}_{\mathrm{Scap}}$) at the beginning of the control window, to provide a smooth power profile of the supercapacitor, and zero "corrected" battery current, to maintain σI_{Batt} as small as possible. The physical principle of this novel controller is to reduce battery wear through a reduction of the "corrected" battery current. The value of the battery weighting factor in Q is equal to 1. The supercapacitor weighting factor is a function of $\mathrm{SOC}_{\mathrm{Scap}}$, to limit and/or prevent a quick discharge of the supercapacitor. For the simulations presented in this paper the weighting factor matrix R has been set at zero.

Once the optimal ΔP_{Batt} has been calculated, the algorithm computes the optimal battery power:

$$P_{\mathrm{Batt\_Opt}}(k) = \Delta P_{\mathrm{Batt\_Opt}}(k) + P_{\mathrm{Batt}}(k-1) \tag{37}$$

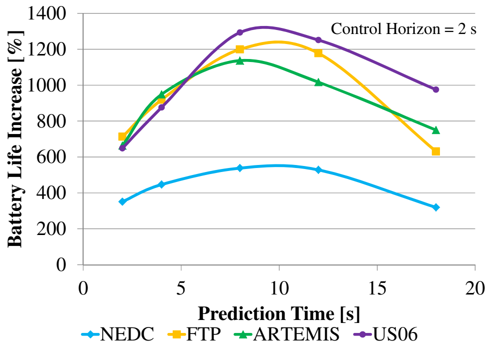

Fig. 14. Battery life increase as function of the MPC prediction time for the different driving cycles.

The sample time of the MPC has been set at 0.5 s in order to achieve a low computational cost, comparable to the one of the rule-based algorithm. During the controller implementation phase, a comparison of the same MPC for the sample times of 0.5 s and 0.01 s has shown a negligible variation of the results, with a significant increase of the required simulation time in the case of 0.01 s. Moreover, the battery life increase predicted for the different driving missions as a function of the prediction time and control horizon is reported in the sensitivity analyses of Figs. 14 and 15. The predicted battery life peaks for prediction times of about 10 s for all the driving schedules, while it experiences an asymptotic behaviour as function of the control horizon. Following this analysis, the prediction time and the control horizons have been set at 10 s.

3.3. Dynamic programming

A dynamic programming algorithm (Fig. 16) has been implemented to understand the potential benefits of a global optimization through the whole driving cycle. The discretization has been carried out according to the supercapacitor state of charge, SOC_{Scap}. The costs at each grid point are calculated for each discrete time (k) and consequently the path with the minimum cost (i.e. optimal control policy) is selected proceeding backwards [43].

The cost function (Eq. (38)) is defined to minimize the overall battery wear along the driving cycle:

$$J_{DP,\ optimal} = \min\left[\sum_{k=0}^{t\_sim} \sigma(I_{Batt},\ T_{Batt},\ SOC_{Batt})|I_{batt}(k)|\right] \tag{38}$$

where $\sigma(I_{Batt},T_{Batt},SOC_{Batt})$ is the severity factor (Eq. (12)).

The models adopted for the DP control action are the same as the simplified ones adopted for the MPC (Figs. 12 and 13). In order

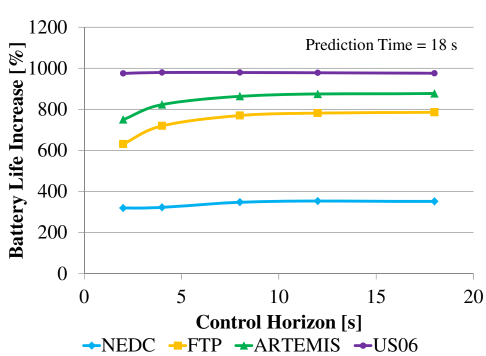

Fig. 15. Battery life increase as function of the MPC control horizon for the different driving cycles.

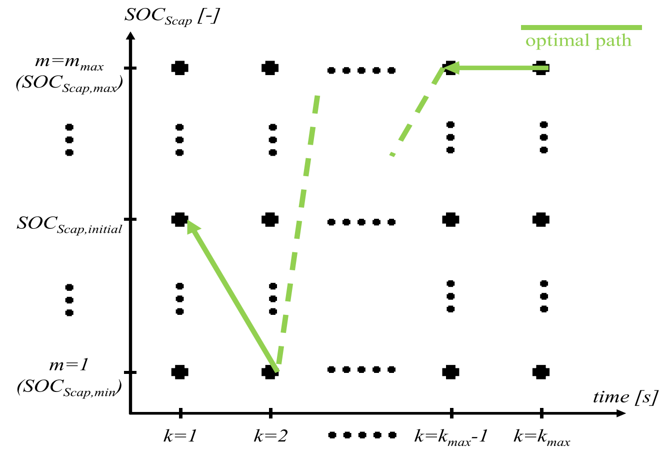

Fig. 16. Dynamic programming schematic with a simplified grid (k indicates the time step and m indicates the value of SOC_{Scap}).

to evaluate the cost for each discretization point (in terms of time and SOC_{Scap}), the supercapacitor power is calculated according to:

$$P_{Scap}(k,m,i) = P_{Scap\_cap}(k,m,i) + P_{Scap\_res}(k,m,i) \tag{39}$$

where $P_{Scap\_cap}(k,m,i)$, defined in Eq. (40), is the power at the capacitance required for the variation of SOC_{Scap} from the value corresponding to the generic discretization point i at the sample time $k-1$ to the discretization point m at the sample time k. $P_{Scap\_res}(k,m,i)$, Eq. (41), is the consequent power dissipation on the supercapacitor resistor due to the variation of SOC_{Scap}.

$$\begin{aligned} P_{Scap\_cap}(k,m,i) = \frac{1}{2}C_{Scap}\Big[&\left(SOC_{Scap}(k,m)V_{c,\ max}\right)^2 \\ &- \left(SOC_{Scap}(k-1,i)V_{c,\ max}\right)^2\Big] \end{aligned} \tag{40}$$

$$\begin{aligned} P_{Scap\_res}(k,m.i) = R_{Scap}\Big[&C_{Scap}\big(SOC_{Scap}(k,m)V_{c,\ max} \\ &-SOC_{Scap}(k-1,i)V_{c,\ max}\big)\Big]^2 \end{aligned} \tag{41}$$

Subsequently, the battery power can be expressed as:

$$P_{Batt}(k,m,i) = P_{HESS}(k) - P_{Scap}(k,m,i)\gamma \tag{42}$$

$$\gamma = \eta^r_{DC/DC} \tag{43}$$

where $\eta_{DC/DC}$ is the lumped efficiency of the DC/DC converter, and $r = \pm 1$ depending on the sign of the supercapacitor power P_{Scap}. The power profile of the hybrid energy storage $P_{HESS}(k)$ is derived from a simulation with the vehicle model and the ECMS high-level controller detailed in Section 2. Once the battery power has been determined, the current (Eq. (44)) and the severity factor (Eq. (45)) can be evaluated in order to calculate the equivalent cost.

$$I_{Batt}(k,m,i) = \frac{-E_{Batt} + \sqrt{E^2_{Batt} + 4R_{Batt}P_{Batt}(k,m,i)}}{2R_{Batt}} \tag{44}$$

$$\sigma = \sigma(I_{Batt}(k,m,i), T_{Batt}(k,m,i), SOC_{Batt}(k,m,i)) \tag{45}$$

The number of discrete points (range of m) for SOC_{Scap} has been set at 300 between the minimum (50%) and the maximum (100%) values allowable for the variable.

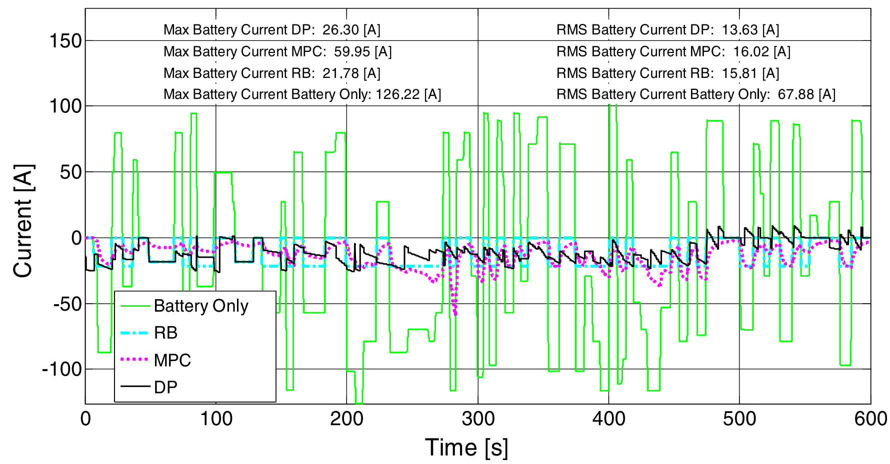

Fig. 17. Battery current profiles during the US06 driving cycle: comparison between battery only, RB, MPC and DP.

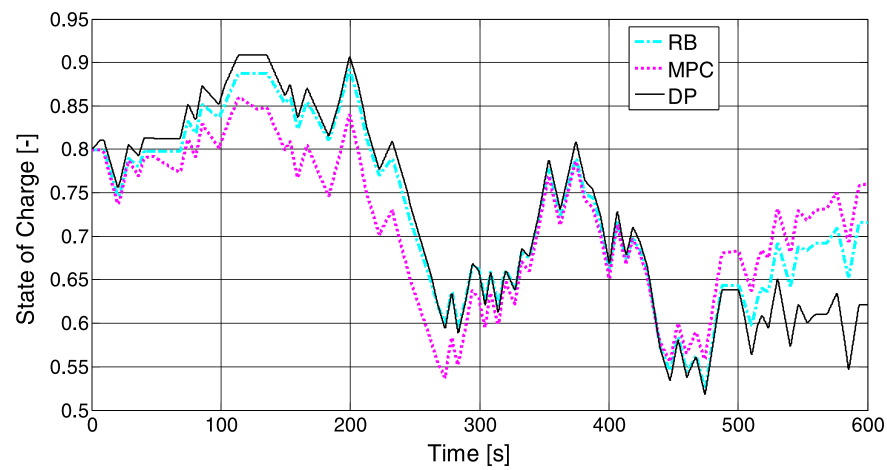

Fig. 18. Supercapacitor state of charge during the US06 driving cycle: comparison between RB, MPC and DP.

Once the map with all the feasible points and the related cost is completed, the controller determines the power split, in particular the power to be sent to the battery, by minimizing the cost function J_{DP}. The sample time for the computation of the optimal control policy has been set at 1 s for the results presented in this article, in order to achieve a low computational cost.

4. Simulation results

Figs. 17–19 show the simulation results during the Supplemental Federal Test Procedure US06 (US06) for the different control algorithms presented in Section 3. The RB and MPC results derive from the implementation of the controllers in the vehicle simulator

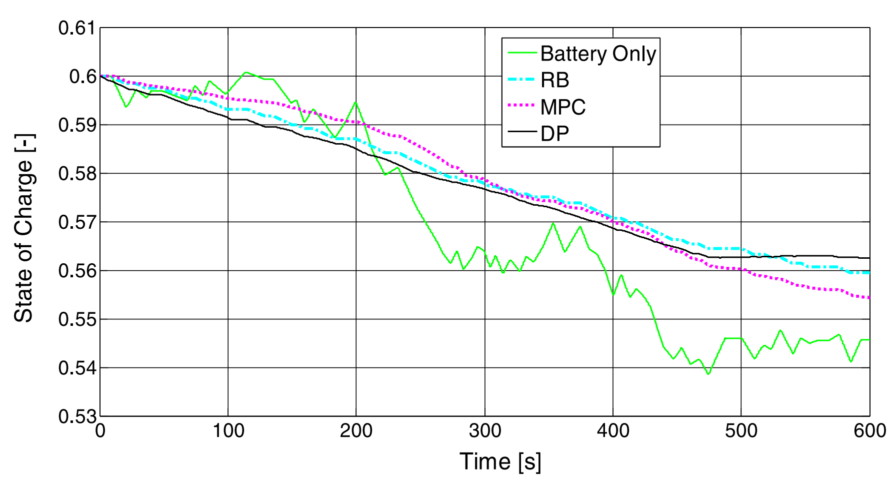

Fig. 19. Battery state of charge during the US06 driving cycle: comparison between battery only, RB, MPC and DP.

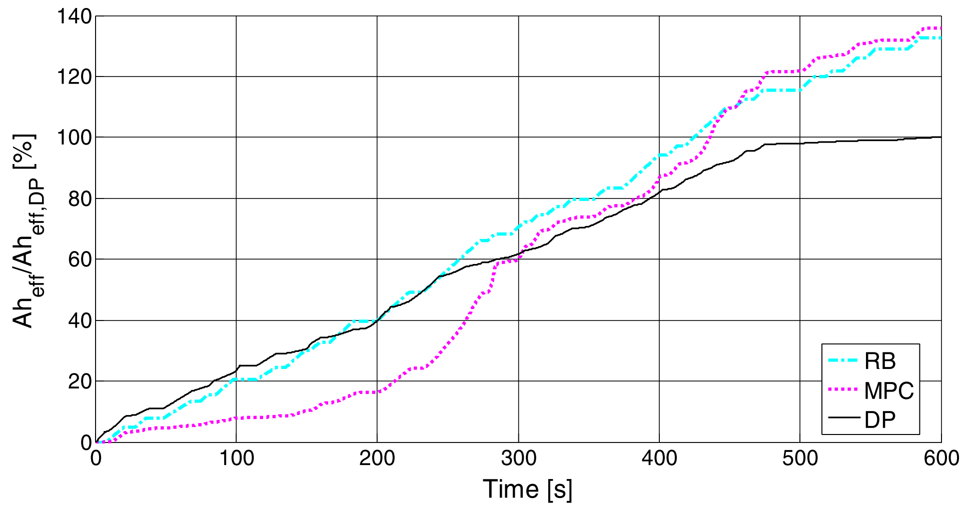

Fig. 20. Normalised battery wear [%] along the US06 driving cycle: comparison between RB, MPC and DP.

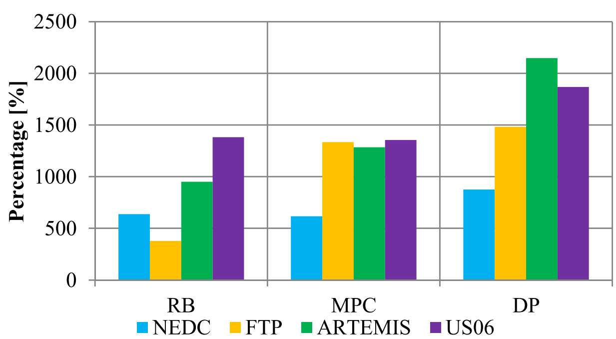

Fig. 21. Percentage of life increase for the different algorithms and driving cycles.

presented in Section 2. In order to fairly compare the DP algorithm results with those from the other controllers, a look-up table describing the optimal battery power profile obtained from the off-line optimisation procedure has been derived and input into the simulation model of Section 2. The supercapacitor initial state of charge is set at 80%.

The battery current profile together with the peak and the RMS values for the different controllers along the US06 driving schedule are reported in Fig. 17. It is worth noticing the difference between the DP and the other controllers for positive battery currents (i.e. recharge condition), in which the DP recharges the battery, whilst the RB and the MPC assign all the recharging power to the supercapacitor stack.

The supercapacitor state of charge for the different control algorithms is reported in Fig. 18. The plot shows that the DP algorithm and the RB controller maintain a higher supercapacitor state of charge for a large portion of the driving schedule compared to the MPC. These comments can be inverted for the battery state of charge reported in Fig. 19, for which, however, the DP produces a higher final state of charge as a consequence of the recharging power sent to the battery stack, as discussed earlier.

Fig. 20 shows the normalised battery wear for the different controllers (RB, MPC and DP) along the same driving cycle. As expected, DP represents the optimal solution achieving the lowest value of battery ageing (corresponding to $Ah_{eff,DP}$) despite the significant battery wear profile in the first portion of the driving cycle. The MPC generates a lower normalised battery wear until the supercapacitor state of charge approaches its lower boundary. Starting from that point, the MPC battery wear significantly increases.

The predicted battery life increase is summarised in Fig. 21. Table 6 reports the detailed results for the New European Driving Cycle (NEDC) and for the Federal Test Procedure (FTP75) driving cycle, while Table 7 reports the overall results for the ‘Assessment and Reliability of Transport Emission Models and Inventory Systems’ (ARTEMIS) and US06 driving cycles. The previous tables are derived for nominal thermal conditions of the drivetrains and the HESS. The adoption of the supercapacitor significantly extends battery life, reducing the RMS and maximum battery current, but it does not improve the overall efficiency of the system (notice the values of power loss in the tables), mainly because of the power losses in the DC/DC converter.

The supercapacitor-to-HESS power split distribution along the US06 driving cycle is shown in Fig. 22. It is worth noticing: i) the linear distribution between the supercapacitor and the overall HESS power, suggesting that a set of rules might be derived from

Table 6
Results for the different options along the NEDC and FTP75 driving schedules.

Parameter	NEDC				FTP75				Unit
	Battery only	RB	MPC	DP	Battery only	RB	MPC	DP	
Max battery current	120	106	71	23	127	106	41	19	[A]
RMS battery current	41	14	14	12	42	18	10	10	[A]
Battery dissipation	205	24	25	17	331	60	19	17	[Wh]
DC/DC converter dissipation	–	187	219	240	–	313	445	477	[Wh]
Supercapacitor dissipation	–	18	20	25	–	16	34	42	[Wh]
Battery life increase	–	637	618	877	–	378	1334	1481	[%]

Table 7
Results for the different options along the ARTEMIS and US06 driving schedules.

Parameter	ARTEMIS				US06				Unit
	Battery only	RB	MPC	DP	Battery only	RB	MPC	DP	
Max battery current	273	159	109	35	126	22	60	26	[A]
RMS battery current	86	27	22	17	68	16	16	14	[A]
Battery dissipation	798	77	54	31	280	15	16	11	[Wh]
DC/DC converter dissipation	–	507	544	603	–	230	256	268	[Wh]
Supercapacitor dissipation	–	69	69	80	–	27	31	35	[Wh]
Battery life increase	–	951	1285	2147	–	1381	1355	1868	[%]

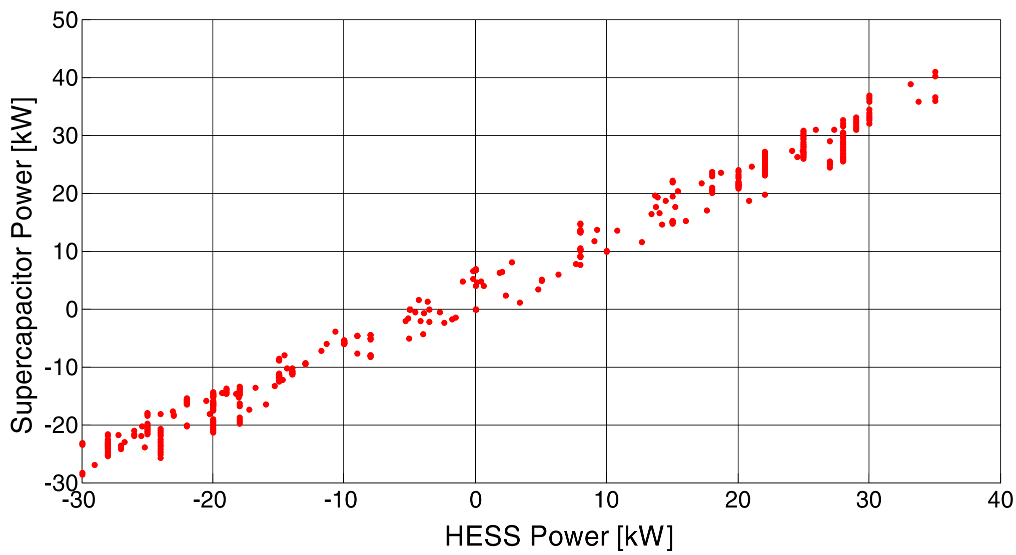

Fig. 22. Power split distribution along the US06 driving cycle.

the DP algorithm, and ii) the presence of points with a positive supercapacitor power in excess of the corresponding HESS power, demonstrating that the battery supplies extra amounts of power in order to recharge the supercapacitor, as confirmed by Fig. 23. This condition is neither discussed nor implemented in RB strategies or other controllers, which send the supercapacitor stack only the power available from regenerative phases.

Linear power distributions also result from the DP algorithm applied to the other (i.e. ARTEMIS, FTP75 and NEDC) driving cycles, here omitted for brevity. A linear approximation of the scatter plots of the power split distributions can be expressed as in Eq. (46):

$$P_{\text{Scap}} = aP_{\text{HESS}} + b \tag{46}$$

The values of a and b for the driving cycles simulated in this paper are reported in Table 8.

5. Conclusions

Three control algorithms for the power split within a HESS of a TTRP HEV have been presented, two of them being newly based on a battery wear model. The simulation results have been discussed and analysed to assess the potential benefits deriving from the

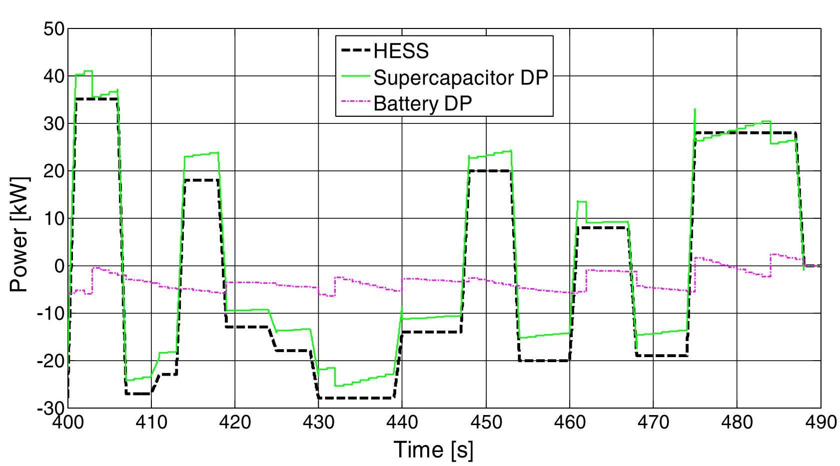

Fig. 23. DP power split: detail of the US06 driving schedule.

Table 8
Linear regression of the power split between HESS and supercapacitor.

	a [–]	b [W]
NEDC	0.94	2376
FTP	0.97	1997
ARTEMIS	0.96	3657
US06	0.97	2964
Average	0.96	2749

adoption of a HESS. In particular, the study demonstrates that a significant decrease of battery wear and RMS and peak values of battery current can be achieved through hybrid energy storage, whilst the adoption of the supercapacitor does not improve the overall energy efficiency of the system in nominal thermal conditions, because of the losses in the DC/DC converter. The rule-based controller allows a 67% reduction of the RMS values of battery current along a selection of driving cycles in comparison with the same vehicle equipped with battery only. In the same conditions the battery peak current is reduced by 38%. The model predictive controller and the dynamic programming algorithm bring an additional reduction of the root mean square value of 6% and 10% respectively, whilst the peak values are additionally decreased by 17% and 45%.

The recommended future developments are: i) to define a set of rules starting from the DP algorithm results in order to design an enhanced rule-based controller, and ii) to implement a computationally efficient DP-derived algorithm using the information from the cloud and the vehicle infotainment system.

Acknowledgements

The research is part of the FP7 project AUTOSUPERCAP, funded by the European Commission under the grant agreement no. 266097.

References

[1] D. Cericola, P. Ruch, R. Kötz, P. Novák, A. Wokaun, J. Power Sources 195 (9) (2010) 2731–2736.
[2] S. Fiorenti, J. Guanetti, Y. Guezennec, S. Onori, J. Power Sources 241 (2013) 112–120.
[3] L. Gao, R.A. Dougal, S. Liu, IEEE Trans. Power Electron. 20 (1) (January 2005) 236–243.
[4] A. Baisden, A. Emadi, IEEE Trans. Veh. Technol. 53 (2004) 199–205.
[5] C. Mi, M. Abul Masru, D.W. Gao, Hybrid Electric Vehicle – Principles and Application with Practical Perspectives, John Wiley & Sons, Ltd, 2011.
[6] L. Gao, R. Dougal, S. Liu, in: Applied Power Electronics Conference and Exposition, 2003.
[7] G. Guidi, T. Undeland, Y. Hori, in: IEEE Power Electronics Specialists Conference, 2007.
[8] R.M. Schupbach, J.C. Balda, in: IEEE International Electric Machines and Drives Conference, 2003.
[9] S. Fui Tie, C. Wei Tan, Renew. Sustain. Energy Rev. 20 (2013) 82–102.
[10] J. Cao, A. Emadi, IEEE Trans. Power Electron. 27 (2012) 122–132.
[11] M. Ortuzar, J. Moreno, J. Dixon, IEEE Trans. Ind. Electron. 54 (2007) 2147–2156.
[12] E. Vinot, R. Trigui, Energy Convers. Manag. 76 (2013) 437–452.
[13] A.H. Eghbali, B. Asaei, P. Nader, in: Vehicle Power and Propulsion Conference, 2010.
[14] M. Masih-Tehrani, M. Ha'iri-Yazdi, V. Esfahanian, A. Safaei, J. Power Sources 244 (2013) 2–10.
[15] R. Karangia, M. Ahmedabad Jadeja, C. Upadhyay, H. Chandwani, in: International Conference on Energy Efficient Technologies for Sustainability (ICEETS), Nagercoil, 2013.
[16] R. Carter, A. Cruden, P.J. Hall, IEEE Trans. Veh. Technol. 61 (4) (May 2012) 1526–1533.
[17] G. Papazov, D. Pavlov, J. Power Sources 62 (1996) 193–199.
[18] G. Randolf, Final Report of the Battery Life Extension Experiment, University of Hawaii, 1999.
[19] H. Wenzl, I. Baring-Gould, R. Kaiser, B.Y. Liaw, P. Lundsager, J. Manwell, A. Ruddell, V. Svoboda, J. Power Sources 144 (2005) 373–384.
[20] N. Omar, M.A. Monema, Y. Firouz, J. Salminen, J. Smekens, O. Hegazy, H. Gaulous, G. Mulder, P. Van den Bossche, T. Coosemans, J. Van Mierlo, Appl. Energy 113 (2014) 1575–1585.
[21] A. Allegre, A. Bouscayrol, R. Trigui, in: IEEE Vehicle Power and Propulsion Conference, 2009.
[22] M. Hadartz, M. Julander, Battery-supercapacitor Energy Storage, University of Chalmers, Goteborg, 2008.
[23] J. Dixon, M. Ortuzar, IEEE Aerosp. Electron. Syst. Mag. 17 (8) (2002) 16–21.
[24] P. Bubna, S.G. Advani, A.K. Prasad, J. Power Sources 199 (2012) 360–366.
[25] H.A. Borhan, A. Vahidi, in: American Control Conference, Baltimore, 2010.
[26] OpEneR FP7 Project (online). Available: http://www.fp7-opener.eu/ (accessed November 2013).
[27] A. Sorniotti, T. Holdstock, G. Loro Pilone, F. Viotto, S. Bertolotto, M. Everitt, R.J. Barnes, B. Stubbs, M. Westby, Proc. Inst. Mech. Eng. D J. Automob. Eng. 226 (7) (2011) 915–929.
[28] M. Goetz, M.C. Levesley, D.A. Crolla, Proc. Inst. Mech. Eng. D J. Automob. Eng. 219 (8) (2005) 951–963.
[29] K.B. Wipke, M.R. Cuddy, S.D. Burch, IEEE Trans. Veh. Technol. 48 (6) (1999) 1751–1761.
[30] C. Musardo, G. Rizzoni, B. Staccia, in: IEEE Conference on Decision and Control, 2005.
[31] A. Sciarretta, M. Back, L. Guzzella, IEEE Trans. Control Syst. Technol. 12 (3) (2004) 352–363.
[32] L. Xu, M. Ouyang, J. Li, F. Yang, L. Lu, J. Hua, Int. J. Hydrogen Energy 38 (24) (2013).
[33] N. Kim, S. Cha, H. Peng, IEEE Trans. Control Syst. Technol. 19 (5) (2011).
[34] L. Gao, S. Liu, R. Dougal, IEEE Trans. Compon. Packag. Technol. 25 (3) (2002) 495–505.
[35] D. Bernardi, E. Pawlikowski, J. Newman, J. Electrochem. Soc. 132 (1) (1985) 5–12.
[36] L. Serrao, S. Onori, A. Sciarretta, Y. Guezennec, G. Rizzoni, in: American Control Conference, San Francisco, 2011.
[37] R. Faranda, M. Gallina, D. Son, in: International Conference on Clean Electrical Power, Capri, 2007.
[38] M. Ehsani, Y. Gao, A. Emadi, Modern Electric, Hybrid Electric, and Fuel Cell Vehicles, CRC Press.
[39] R. Faranda, Electr. Power Syst. Res. 80 (2010).
[40] J.M. Maciejowski, Predictive Control with Constraints, Pearson Education Limited, 2002.
[41] R. J. Vanderbei (online). Available: http://orfe.princeton.edu/~rvdb/pdf/talks/pumath/talk.pdf (accessed 06.12.13).
[42] N. Gould (online). Available: http://www.numerical.rl.ac.uk/people/nimg/course/lectures/parts/part4.2.pdf (accessed 06.12.13).
[43] D.E. Kirk, Optimal Control Theory – an Introduction, Dover Publications, Inc, 1998.